

Quantitative subsurface contact resonance force microscopy of model polymer nanocomposites*

Jason P Killgore¹, Jennifer Y Kelly², Christopher M Stafford²,
Michael J Fasolka³ and Donna C Hurley¹

¹ Materials Reliability Division, National Institute of Standards and Technology, Boulder, CO, USA

² Polymers Division, National Institute of Standards and Technology, Gaithersburg, MD, USA

³ Material Measurement Laboratory, National Institute of Standards and Technology, Gaithersburg, MD, USA

E-mail: killgore@nist.gov

Received 25 October 2010, in final form 7 February 2011

Published 16 March 2011

Online at stacks.iop.org/Nano/22/175706

Abstract

We present experimental results on the use of quantitative contact resonance force microscopy (CR-FM) for mapping the planar location and depth of 50 nm diameter silica nanoparticles buried beneath polystyrene films 30–165 nm thick. The presence of shallowly buried nanoparticles, with stiffness greater than that of the surrounding matrix, is shown to locally affect the surface contact stiffness of a material for all depths investigated. To achieve the necessary stiffness sensitivity, the CR-FM measurements are obtained utilizing the fifth contact eigenmode. Stiffness contrast is found to increase rapidly with initial increases in force, but plateaus at higher loads. Over the explored depth range, stiffness contrast spans roughly one order of magnitude, suggesting good depth differentiation. Scatter in the stiffness contrast for single images reveals nonuniformities in the model samples that can be explained by particle size dispersity. Finite element analysis is used to simulate the significant effect particle size can have on contact stiffness contrast. Finally, we show how measurements at a range of forces may be used to deconvolve particle size effects from depth effects.

 Online supplementary data available from stacks.iop.org/Nano/22/175706/mmedia

(Some figures in this article are in colour only in the electronic version)

1. Introduction

In nanocomposite systems, the dispersion of nanoparticles is critical in determining the resultant properties (e.g. mechanical [1], electrical [2], transport [3]) of a material. While topographic measurements with scanning probe or electron microscopy can provide information regarding the in-plane surface dispersion of nanoparticles [4], such techniques do not readily provide quantitative information about through-thickness dispersion. By cross-sectioning the samples, through-thickness information can be obtained; however, the process is destructive and extremely time consuming

* Publication of NIST, an agency of the US government, not subject to copyright.

when high-resolution tomographic reconstruction is required. Thus, a need exists for efficient, nondestructive methods of characterizing nanoparticle dispersion in nanocomposites.

Although originally developed as a surface topographic measurement tool [5], the atomic force microscope (AFM) has more recently been extended to subsurface characterization methods [6–13]. Acoustic [6, 7], electric [8, 9], and stiffness [10–13] based AFM contrast mechanisms have been used to elicit subsurface information. Acoustic ultrasound based approaches rely on phase contrast in high frequency (>1 MHz) waves that propagate through a sample with subsurface features and are detected at the surface [6, 7]. While such methods have been used to resolve buried features at large depths (500 nm–5 μ m), the underlying physics is still not well

understood. Thus, they are not yet suitable for quantitative depth differentiation, but for qualitative visualization only.

For a stiffness based subsurface characterization method, contrast arises from the difference in modulus between the matrix and an inclusion [12]. When an AFM tip is brought into contact with a surface, the resulting stress field extends into the material. The extent of the stress field depends on the stiffness of the tip and sample, the size and shape of the tip, and the applied force [14]. If the stress field extends deeply enough to probe an inclusion, and the stiffness of the inclusion differs from that of the surrounding matrix, the stiffness of the surface will be locally changed. Such an approach has been modeled by Degertekin and co-workers [12]. Using finite element analysis, they demonstrated that AFM techniques for measuring contact stiffness k could be used to quantitatively determine the size and depth of buried inclusions or voids in a silicon matrix. Their model was validated on a subsurface void of known location in silicon. Atomic force acoustic microscopy (AFAM) point measurements were made across the surface above the void to measure local stiffness variations.

Because polymeric nanocomposites often employ a rigid inorganic filler (modulus E from 50 to 1000 GPa) in a compliant polymer matrix (E from 0.1 to 10 GPa), a high stiffness contrast should exist between matrix and filler. Here, we used contact resonance force microscopy (CR-FM) mapping techniques to locate buried nanoparticles in a polymer matrix. With CR-FM mapping techniques, we were able to achieve similar stiffness sensitivity to that obtained by pointwise AFAM, but with the required speed and spatial resolution to detect and measure buried nanostructures at unknown locations. To resolve depth dependence, samples were fabricated such that the particles were positioned beneath a cover film of known thickness. From the CR-FM results, we determined the difference in contact stiffness between neat polymer and buried particle as a function of film thickness and applied force. Practical aspects of implementing polymer nanocomposite tomography were investigated, and the results were further interpreted with finite element analysis.

2. Experimental methods and procedures⁴

2.1. Sample preparation

A schematic of a model sample is shown in figure 1. The samples consisted of a silicon substrate, a thick polystyrene (PS) base film, and a discrete layer of nanoparticles buried beneath a thinner PS cover film. The samples were prepared by first spin casting a 10 wt% solution of PS (weight average molecular weight $M_w = 250\,000\text{ g mol}^{-1}$, number average molecular weight $M_n = 150\,000\text{ g mol}^{-1}$) onto a toluene and ultraviolet/ozone (UVO) cleaned silicon wafer at 209 rad s^{-1} (2000 rpm), producing a film with thickness $T \approx 1.4\ \mu\text{m}$. Next, the films were annealed for 1 h at $150\text{ }^\circ\text{C}$ under vacuum. To promote adhesion of the nanoparticles, the films were

⁴ Commercial equipment, instruments, or materials are identified only in order to adequately specify certain procedures. In no case does such identification imply recommendation or endorsement by the National Institute of Standards and Technology, nor does it imply that the products identified are necessarily the best available for the purpose.

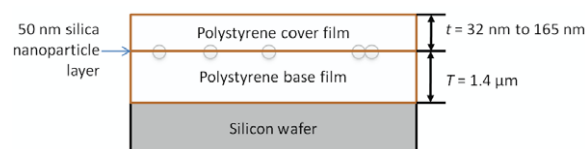


Figure 1. Schematic of the model nanocomposite. Nanoparticles are spun cast atop a thick polystyrene substrate, then covered with a thin polystyrene film and annealed.

exposed to 10 min of UVO treatment. Silica nanoparticles with nominal diameter $\varnothing = 50\text{ nm}$ (Snowtex, Nissan Chemical, Houston, TX) were then spun cast onto the base film from a 0.025% solution in water. AFM analysis of the size distribution of particles showed a mean diameter of $(50.6 \pm 8.2)\text{ nm}$, where the uncertainty represents one standard deviation (see figure S1, supplementary information available at stacks.iop.org/Nano/22/175706/mmedia). In order to sink the particles into the substrate film, the specimens were placed back in the vacuum oven at $150\text{ }^\circ\text{C}$ for 5 min. Cover films were prepared from more dilute (1%–3%) solutions of the same PS, with spin speeds from 105 to 315 rad s^{-1} (1000–3000 rpm), yielding films of thickness $t = 32, 53, 76, 92, 125,$ and 165 nm (measured with interferometry and confirmed with AFM). To allow easier release of the films, no UVO treatment was applied to the silicon substrates during fabrication of the cover films. The cover films were released from their substrate by scoring the edges and immersing in water. The nanoparticle-covered base films were then placed underneath the floating films and withdrawn. Finally, the complete assemblies were annealed for 14 h at $150\text{ }^\circ\text{C}$.

2.2. Contact resonance force microscopy

CR-FM measurements are well explained in the literature [15–17]. Briefly, measurements for the n th contact eigenmode are obtained by bringing the AFM tip into contact with the surface under investigation, then exciting the cantilever (directly or with a transducer beneath the sample) over a range of frequencies bracketed by the n th and $n + 1$ th free air resonance frequencies. It is possible to model the cantilever in contact with the sample as a distributed mass beam with one end clamped at the cantilever holder and a spring representing the tip–sample contact located some finite distance from the beam’s end. With knowledge of the n th free air resonance, the contact resonance frequency f_n^c can be quantitatively related to the contact stiffness k of the tip–sample spring. By continuously measuring f_n^c during contact scanning, it is possible to obtain simultaneous images of contact stiffness and topography.

All CR-FM experiments were performed on an MFP-3D instrument (Asylum Research, Santa Barbara, CA); however, the general approach should be widely applicable to any AFM with access to the photodiode signal. High-resolution mapping of the contact resonance frequency was performed with a modified version of the previously described, NIST-developed scanning probe resonance image tracking electronics (SPRITE) [18]. During contact-mode scanning, the

SPRITE circuit continually sweeps the excitation frequency over a window 25–64 kHz wide, while an RMS detector on the photodiode is used to monitor cantilever motion. To enable high-resolution tracking of large frequency shifts, feedback control is used to continuously center the sweep window around the resonance frequency f_n^c . Key differences between the previously reported circuit and the electronics used in this study include direct digital synthesis of the waveform, the ability to set hard limits on the frequency range under investigation, and the ability to map an arbitrarily sized frequency range onto the ± 10 V output.

All measurements were made with a rectangular cantilever with nominal dimensions of length $L = 450 \mu\text{m}$, width $w = 50 \mu\text{m}$, and thickness $b = 2 \mu\text{m}$. The measured values of the fundamental free resonance frequency f_1^0 and the fifth free resonance frequency f_5^0 were (10.5 ± 0.1) kHz and (605.4 ± 0.1) kHz, respectively. With the AFM's built-in routine, thermal calibration of the cantilever yielded a cantilever spring constant $k_L = (0.11 \pm 0.01) \text{ N m}^{-1}$. Prior to the subsurface experiments, the tip was scanned on a silicon substrate to deliberately wear the tip, yielding a larger radius that would provide deeper sensing and be less prone to additional changes during the experiments [14, 19]. A lack of additional wear during subsurface imaging was indicated by a relatively constant contact resonance frequency on the blank polymer matrix regions throughout the scan. After subsurface imaging, scanning electron microscope (SEM) characterization of the AFM tip apex showed a radius $R_{\text{SEM}} = 150 \text{ nm}$ (see figure S2, supplementary information available at stacks.iop.org/Nano/22/175706/mmedia).

CR-FM maps were obtained as a function of eigenmode, applied load, and particle depth. For the eigenmode study, frequency maps were acquired on the 92 nm thick cover film sample for the first five eigenmodes to determine the mode with optimal sensitivity for subsurface detection [20]. With the optimal eigenmode, CR-FM maps were obtained for each thickness t of surface film at total loads F from 4.5 to 79 nN, determined from the sum of the applied force and adhesion force. For all CR-FM measurements, regions for investigation were randomly chosen, with final measurements obtained on $3 \mu\text{m}$ square regions at a scan rate of 0.3 Hz. Following the methodology of Rabe *et al* [16], the tip position as a percentage of cantilever length L_1/L was determined by solving the distributed mass model for two different eigenmodes (4 and 5 in this case) and calculating the tip position where the contact stiffnesses are equal. This resulted in a calculated value of $L_1/L = 0.974$, which was used to convert frequency maps into contact stiffness maps. The contact stiffness contrast $\Delta k/k_b$ between a buried particle and the matrix was then defined by

$$\frac{\Delta k}{k_b} = \frac{k_p - k_b}{k_b}, \quad (1)$$

where k_p is the on-particle contact stiffness measured at the particle apex and k_b is the average contact stiffness of the particle-free matrix regions.

2.3. Finite element modeling

To gain additional insight into the contact stiffness measurements, finite element analysis (FEA) was used. ANSYS

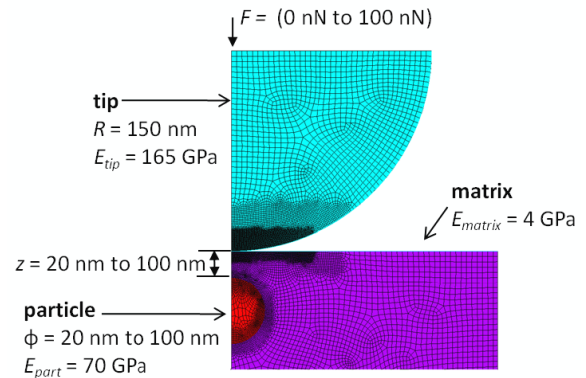


Figure 2. Finite element model of the AFM tip-buried particle system. Geometry is defined by tip radius R , particle diameter ϕ , and particle depth z . Load F is applied to the center of the tip. z and ϕ were varied to determine their effects on observed contact stiffness. Material moduli E_{tip} , E_{part} , and E_{matrix} were chosen to be close to the expected properties of the model experimental samples. A Poisson's ratio ν of 0.3 was assumed for all materials.

(Canonsburg, PA) axisymmetric finite element models were used to study the effects of buried particle size and depth on the observed contact stiffness. Tip, matrix, and nanoparticle were all modeled with eight-node two-dimensional (2D) elements (PLANE82). Based on the SEM results, the tip was modeled as a silicon hemisphere of radius $R = 150 \text{ nm}$, as shown in figure 2. The matrix was represented as a 300 nm tall cylinder with 200 nm radius. An embedded spherical particle of diameter ϕ was located along the y -axis of the cylinder, with its top located a prescribed depth z from the surface. Initially, all elements were automatically meshed with the preprocessor's fine smart-size function. Further refinement was implemented near the tip-sample contact and the buried particle-matrix interface. Contact between the tip and matrix was handled with a symmetric pair of surface-to-surface contact elements (TARGE169 and CONTA172). The particle-matrix interface was modeled as perfectly bonded by use of coincident nodes. For simplicity, all materials were modeled as isotropic and linearly elastic, with properties given in figure 2. Displacement of the tip was dictated by a 100 nN load applied on the y -axis at the top plane of the hemisphere and solved in incremental force substeps $\Delta F = 1 \text{ nN}$ with large deformation analysis enabled. The y -motion of the top plane of the tip was coupled. Contact stiffness k as a function of load F was determined by

$$k(P) = \frac{\partial F}{\partial d} \cong \frac{1}{2} \left(\frac{F_i - F_{i-\Delta F}}{d_i - d_{i-\Delta F}} + \frac{F_{i+\Delta F} - F_i}{d_{i+\Delta F} - d_i} \right), \quad (2)$$

where F_i is the applied force at load step i and d_i is the corresponding observed tip displacement. Models were created for depths $z = 20, 50, \text{ and } 100 \text{ nm}$ with a constant $\phi = 50 \text{ nm}$ diameter particle. To investigate the effects of particle size, models were also prepared with 20, 50, 100 nm, and infinite (flat plane) diameter particles at a fixed depth $z = 50 \text{ nm}$. The on-particle contact stiffness k_p was compared to the blank matrix contact stiffness k_b by re-solving the same models, but with the properties of the particle set equal to the matrix.

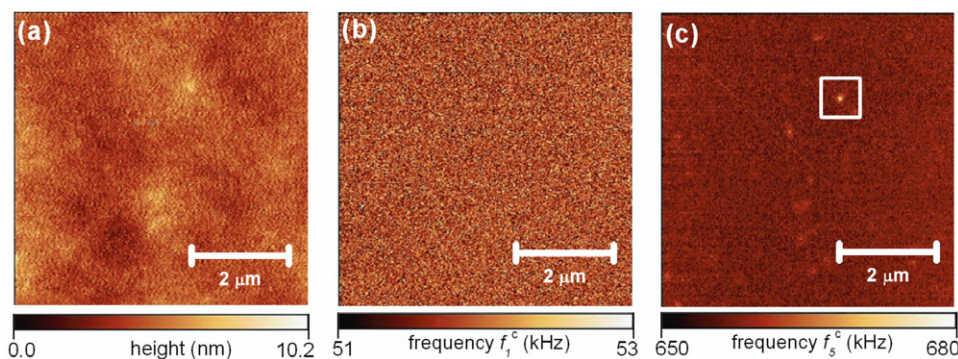


Figure 3. (a) Topography, (b) first eigenmode CR-FM, and (c) fifth eigenmode CR-FM images acquired on the $t = 92$ nm sample. The images in (a) and (b) were acquired simultaneously. The image in (c) was acquired without modifying the scan location. Correlated topographic features confirmed that the same area was measured in all images. The buried particle outlined in (c) was not resolved with the first eigenmode.

Thus, the contact stiffness contrast could be determined from equation (1).

3. Results and discussion

3.1. Eigenmode selection

Contact-mode imaging on polymeric surfaces generally requires low applied forces to avoid sample wear and ripple pattern formation. To facilitate precise low-force control, a compliant cantilever was used in this study. As shown in figures 3(a) and (b), CR-FM and topography maps obtained with the first eigenmode on a sample with a 92 nm thick cover film showed no evidence of rigid subsurface structures. As seen in figure 3(c), by tracking the fifth eigenmode while scanning the same area, it was possible to observe a bright, higher-frequency feature with the expected size of a buried nanoparticle. Additional lower-contrast features are also seen in the higher-mode image. The enhanced contrast at higher eigenmodes is attributed to the increased effective stiffness of the higher mode. Based on the distributed-mass model, figure 4 shows the theoretical frequency sensitivity as a function of contact stiffness for the first five eigenmodes of the cantilever under investigation. For the samples used here, the choice of compliant cantilever and large radius tip results in contact stiffness values for which the first eigenmode had insufficient sensitivity to resolve frequency contrast. By comparison, modes 4 and 5 are expected to have sensitivity two orders of magnitude higher than that of mode 1, leading to the contrast in the mode 5 frequency map. Although modes 4 and 5 are both suitable for subsequent measurements, experimentally mode 5 was chosen over mode 4 because it provided a more ideal resonance peak and more reliable tracking. An additional benefit of the higher eigenmodes is that higher-frequency modulation should result in less damping in the polymer matrix, possibly enhancing the depth sensitivity compared to that of lower-frequency measurements.

3.2. Detection of buried particles

Figure 5 shows simultaneously acquired topography and CR-FM stiffness contrast maps obtained on samples with $t = 32$

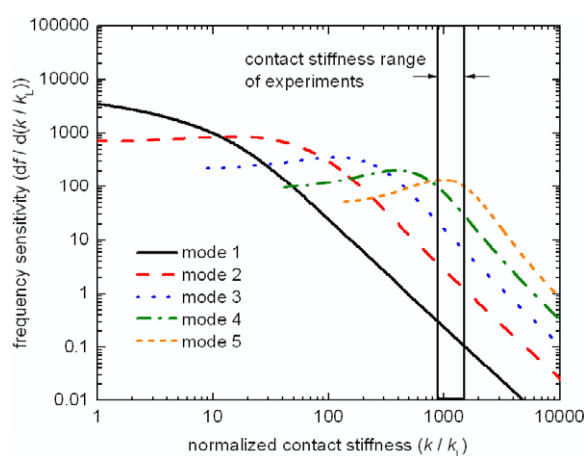


Figure 4. Theoretical frequency sensitivity versus normalized contact stiffness k/k_L . The sensitivity was calculated with the distributed-mass model assuming elastic contact. For the experimental range of contact stiffness indicated by the vertical lines, the use of higher-order eigenmodes provides much greater frequency sensitivity than the first eigenmode.

and 125 nm films covering the buried nanoparticles. For the $t = 32$ nm film (figures 5(a) and (b)), the buried particles are easily discerned in both the topography and the frequency images. The surface topography variations associated with the covered particles range from 20 to 30 nm. Assuming that the observed particles are representative of the 50 nm mean diameter, the observed topography suggests a combination of surface-film-to-particle draping and embedding of the particles into both substrate and cover films. The embedding into the cover film introduces some uncertainty in the absolute depth of the particles. However, given the observed heights of the covered particles and the assumption that embedding occurs both above and below the particle, the depth uncertainty was generally less than 20 nm. In contrast to the $t = 32$ nm sample, no topographic evidence of the particles was seen for particles buried beneath 125 nm of polystyrene (figures 5(c) and (d)). However, the stiffness contrast map shows numerous discrete features with dispersion and size consistent with buried particles. Comparing the samples with 32 and 125 nm

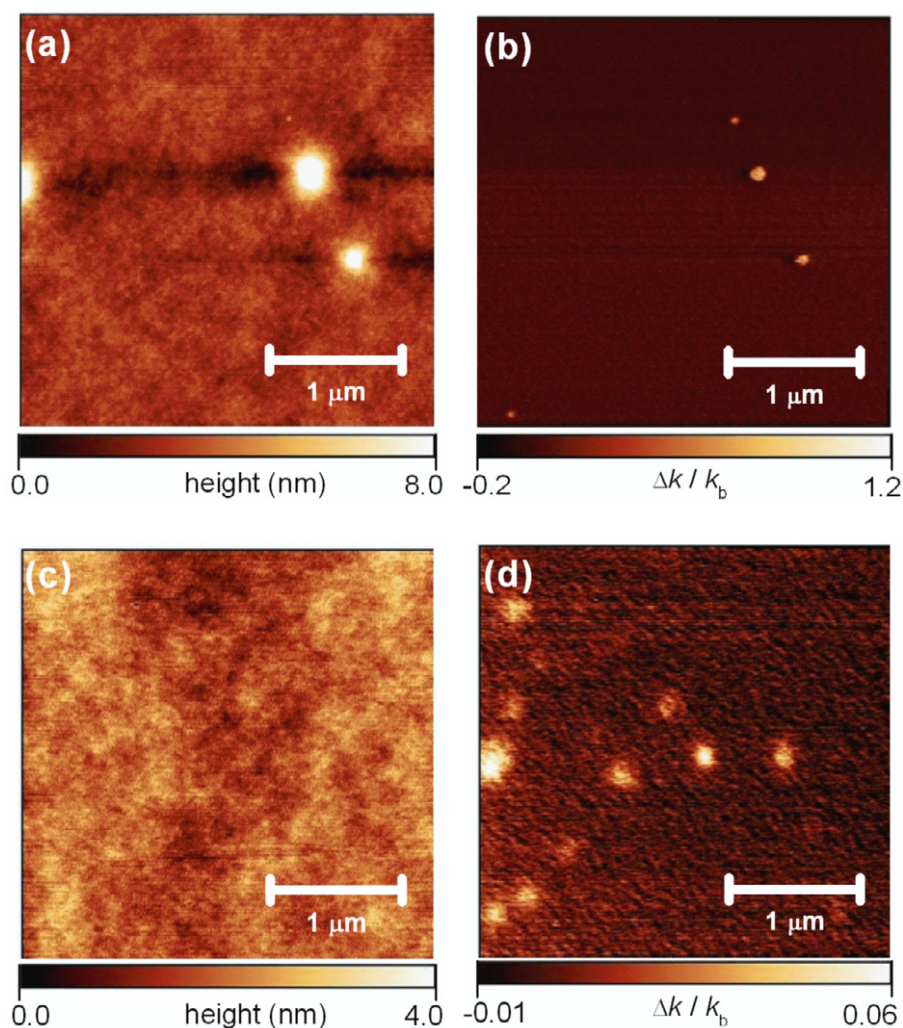


Figure 5. (a), (b) Simultaneously acquired topography and contact stiffness contrast $\Delta k/k_b$ images obtained on model samples with a $t = 32$ nm cover film. (c), (d) Simultaneously acquired topography and contact stiffness contrast images obtained on the model sample with a $t = 125$ nm cover film. All images were acquired with an applied load of 30 nN.

thick films, significantly higher contrast in contact stiffness was observed for shallowly buried particles in the $t = 32$ nm sample compared to the $t = 125$ nm sample. The increased contrast of the shallow particles was expected because the rigid structure occupies the more sensitive near-contact region of the stress field.

In order to experimentally quantify the depth and load dependence of the contact stiffness contrast, multiple images at a range of applied loads were obtained for each sample. The experimental results are summarized in figure 6(a), and corresponding FEA simulation results are shown in figure 6(b). In both cases, contrast generally increased with load and decreased with cover film thickness. For a hemispherical indenter, higher loads were expected to increase the tip-sample contact area. This increased the overall depth of the stress field and allowed the buried particles to affect a larger percentage of the measurement volume. The leveling off of contrast at higher forces was attributed to a stress field that fully encompassed the particle. Thus, further loading showed only slight increase in contrast. This lessened force

dependence is particularly desirable because it allows near-optimal contrast at nondestructive loads. Quantitatively, the FEA model predicted lower contrast for a given depth than was observed experimentally. Some discrepancy may have originated from the uncertainty in the actual nanoparticle depth in the experimental samples discussed above. Other factors contributing to the discrepancy may include imprecisely modeled tip geometry, material properties, or interfacial stress transfer. For example, FEA results assuming tip radius values larger than those experimentally observed predict higher stiffness contrast values than in figure 6(b) (see figure S3, supplementary information available at stacks.iop.org/Nano/22/175706/mmedia).

3.3. Depth differentiation

For tomographic applications, it is necessary to ensure that particle depths can be differentiated. Figure 7 shows the distribution in contact stiffness contrast $\Delta k/k_b$ for measurements on $t = 32$ and 76 nm samples with $F = 41$ nN.

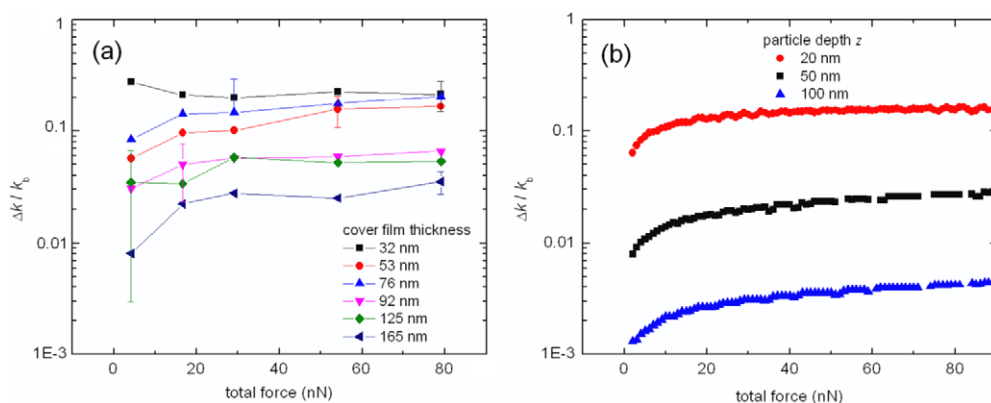


Figure 6. (a) Experimental and (b) FEA results for contact stiffness contrast $\Delta k/k_b$ as a function of total force (applied force plus adhesion) and cover film thickness t or particle depth z . Error bars in (a) are shown for only one force for clarity, but they represent the average standard deviation for all forces at the indicated film thickness. In (b), particle diameter $\phi = 50$ nm. Results from poorly converged load steps have been omitted.

Although the modal values are well separated, the tails on the measurements clearly overlap, presenting the possibility for signal misinterpretation in a true composite where particles have both depth and size dispersity. Experimentally, a sample of 42 nanoparticles showed diameters ranging from 34 to 70 nm (see figure S1, supplementary information available at stacks.iop.org/Nano/22/175706/mmedia). It is likely that a larger sample size would reveal even greater outliers. The FEA results in figure 8(a) simulate how particle size dispersity is expected to affect contact stiffness contrast. For a fixed depth $z = 50$ nm, a change in particle diameter from 20 to 100 nm resulted in more than an order of magnitude increase in contrast. When the diameter was increased to the extent that the particle surface approximated an infinite flat plane, even greater contrast was observed. As a result of size dispersity effects, it is possible that smaller particles may fall below the detection limits of CR-FM while larger particles are more readily detected. Experimentally, this phenomenon may have contributed to the detection of fewer particles for the $t = 165$ nm sample compared to samples with thinner cover films, in spite of the fact that all samples were prepared with nominally identical particle concentrations. It may also explain why the experimental curves in figure 6(a) for more shallowly buried particles showed good agreement with the FEA predictions in figure 6(b), while experiments on more deeply buried particles showed much greater contrast than predicted by FEA. In other words, it is possible that only larger diameter particles were detected in samples with thicker cover films.

Comparing the particle size FEA results in figure 8(a) to the particle depth FEA results in figure 6(b), it is seen that measurement forces exist where an image at a single force will convolute particle size and depth. This is circled in the low-force regime of figure 8(b). Here, the FEA results predict that a $\phi = 20$ nm diameter particle buried $z = 50$ nm deep and a $\phi = 50$ nm particle buried $z = 100$ nm deep will show approximately the same stiffness contrast for $F < 10$ nN. However, by applying higher forces, the particles can be increasingly differentiated. Thus, for real systems, it

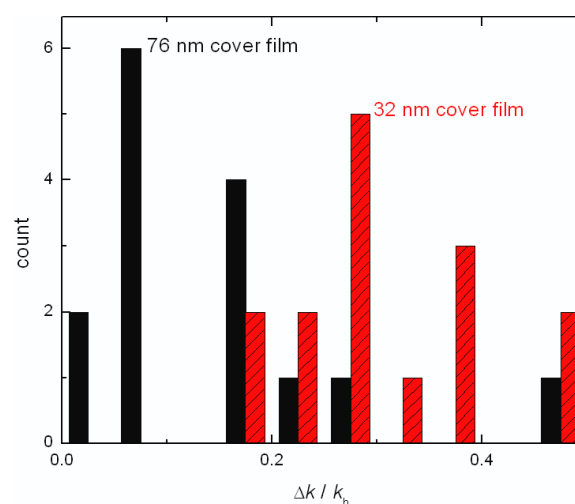


Figure 7. Histogram of contact stiffness contrast $\Delta k/k_b$ for datasets acquired at $t = 32$ nm (striped red) and $t = 76$ nm (solid black) samples with a 41 nN load.

will likely be necessary to obtain measurements at a range of forces. Additional depth differentiation might also be achieved by measuring the observed lateral dimensions of the buried particles in the frequency images. However, this dependence was difficult to resolve for the scan sizes used in this study.

4. Conclusions

CR-FM mapping techniques have been demonstrated for the detection of subsurface silica nanoparticles buried beneath more than 100 nm of polystyrene. Higher-order eigenmodes were used to increase the sensitivity of otherwise compliant AFM cantilevers, allowing stable operation at minimally destructive forces. With a distributed-mass model, the frequency maps were translated into quantitative contact stiffness. This allowed the effect of buried nanoparticles on surface contact stiffness to be quantified as a function of force and depth. FEA modeling suggested that a single contact stiffness map would be sufficient for depth differentiation

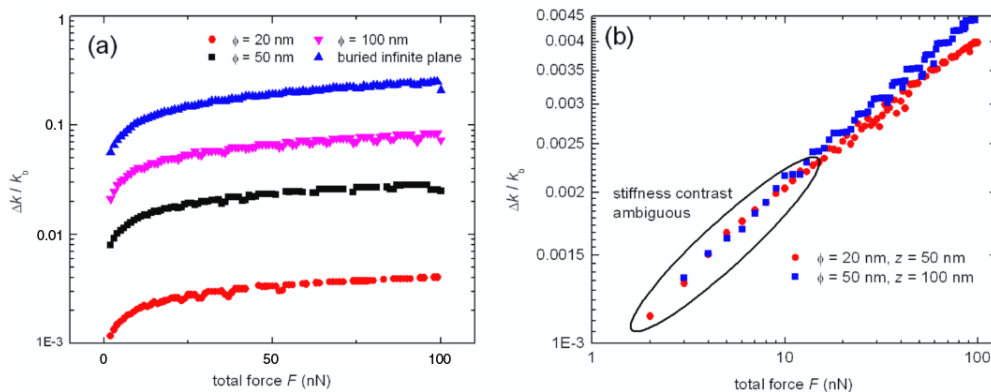


Figure 8. (a) FEA results showing contact stiffness contrast $\Delta k/k_b$ as a function of particle diameter ϕ and force F for depth $z = 50$ nm. (b) FEA results for $\Delta k/k_b$ for a 20 nm diameter particle buried 50 nm deep (red circles) and a 50 nm particle buried 100 nm deep (blue squares). The circled region is the low-force regime where the stiffness contrast of the two particles cannot be differentiated. Results from poorly converged load steps have been omitted.

of monodisperse nanoparticles. However, separate maps at multiple applied forces are likely necessary for characterizing variably sized particles. More complex geometries such as layers of particles may require additional information such as the apparent lateral dimensions of features or coincident use of CR-FM with other subsurface techniques such as electrostatic force microscopy or ultrasound based AFM. Our results on depth profiling of shallowly buried nanoparticles have applications in nanocomposite coatings, where near-surface dispersion may impart specific chemical or wear resistance. Further, because it is generally nondestructive, this approach enables single-sample, systematic, time-dependent, *in situ* and *ex situ* investigations that are not possible with destructive cross-sectioning.

Acknowledgments

This research was performed while JPK and JYK held National Research Council Research Associateship Awards at the National Institute of Standards and Technology.

References

- [1] Yang F, Ou Y C and Yu Z Z 1998 Polyamide 6 silica nanocomposites prepared by *in situ* polymerization *J. Appl. Polym. Sci.* **69** 355–61
- [2] Croce F, Appetecchi G B, Persi L and Scrosati B 1998 Nanocomposite polymer electrolytes for lithium batteries *Nature* **394** 456–8
- [3] Messersmith P B and Giannelis E P 1995 Synthesis and barrier properties of poly(epsilon-caprolactone)-layered silicate nanocomposites *J. Polym. Sci. A* **33** 1047–57
- [4] Huang X Y and Brittain W J 2001 Synthesis and characterization of PMMA nanocomposites by suspension and emulsion polymerization *Macromolecules* **34** 3255–60
- [5] Binnig G, Quate C F and Gerber C 1986 Atomic force microscope *Phys. Rev. Lett.* **56** 930
- [6] Shekhawat G S and Dravid V P 2005 Nanoscale imaging of buried structures via scanning near-field ultrasound holography *Science* **310** 89–92
- [7] Cantrell S A, Cantrell J H and Lillehei P T 2007 Nanoscale subsurface imaging via resonant difference-frequency atomic force ultrasonic microscopy *J. Appl. Phys.* **101** 8
- [8] Takano H, Wong S-S, Harnisch J A and Porter M D 2000 Mapping the subsurface composition of organic films by electric force microscopy *Langmuir* **16** 5231–3
- [9] Zhao M H, Gu X H, Lowther S E, Park C, Jean Y C and Nguyen T 2010 Subsurface characterization of carbon nanotubes in polymer composites via quantitative electric force microscopy *Nanotechnology* **21** 225702
- [10] Yamanaka K, Ogiso H and Kolosov O 1994 Ultrasonic force microscopy for nanometer resolution subsurface imaging *Appl. Phys. Lett.* **64** 178–80
- [11] Sarioglu A F, Atalar A and Degertekin F L 2004 Modeling the effect of subsurface interface defects on contact stiffness for ultrasonic atomic force microscopy *Appl. Phys. Lett.* **84** 5368–70
- [12] Parlak Z and Degertekin F L 2008 Contact stiffness of finite size subsurface defects for atomic force microscopy: three-dimensional finite element modeling and experimental verification *J. Appl. Phys.* **103** 8
- [13] He C F, Zhang G M, Wu B and Wu Z Q 2010 Subsurface defect of the SiO_x film imaged by atomic force acoustic microscopy *Opt. Lasers Eng.* **48** 1108–12
- [14] Johnson K L 1985 *Contact Mechanics* (Cambridge: Cambridge University Press)
- [15] Yamanaka K, Noguchi A, Tsuji T, Koike T and Goto T 1999 Quantitative material characterization by ultrasonic AFM *Surf. Interface Anal.* **27** 600–6
- [16] Rabe U, Amelio S, Kester E, Scherer V, Hirsekorn S and Arnold W 2000 Quantitative determination of contact stiffness using atomic force acoustic microscopy *Ultrasonics* **38** 430–7
- [17] Hurley D C, Shen K, Jennett N M and Turner J A 2003 Atomic force acoustic microscopy methods to determine thin-film elastic properties *J. Appl. Phys.* **94** 2347–54
- [18] Kos A B and Hurley D C 2008 Nanomechanical mapping with resonance tracking scanned probe microscope *Meas. Sci. Technol.* **19** 015504
- [19] Kopycinska-Müller M, Geiss R H and Hurley D C 2006 Contact mechanics and tip shape in AFM-based nanomechanical measurements *Ultramicroscopy* **106** 466–74
- [20] Turner J A and Wiehn J S 2001 Sensitivity of flexural and torsional vibration modes of atomic force microscope cantilevers to surface stiffness variations *Nanotechnology* **12** 322–30